

Curvature-Controlled Defect Localization in Elastic Surface Crystals

Francisco López Jiménez,¹ Norbert Stoop,² Romain Lagrange,² Jörn Dunkel,^{2,*} and Pedro M. Reis^{1,3,†}

¹Department of Civil & Environmental Engineering, Massachusetts Institute of Technology,
77 Massachusetts Avenue, Cambridge, Massachusetts 02139-4307, USA

²Department of Mathematics, Massachusetts Institute of Technology,
77 Massachusetts Avenue, Cambridge, Massachusetts 02139-4307, USA

³Department of Mechanical Engineering, Massachusetts Institute of Technology,
77 Massachusetts Avenue, Cambridge, Massachusetts 02139-4307, USA

(Received 20 September 2015; revised manuscript received 10 February 2016; published 7 March 2016)

We investigate the influence of curvature and topology on crystalline dimpled patterns on the surface of generic elastic bilayers. Our numerical analysis predicts that the total number of defects created by adiabatic compression exhibits universal quadratic scaling for spherical, ellipsoidal, and toroidal surfaces over a wide range of system sizes. However, both the localization of individual defects and the orientation of defect chains depend strongly on the local Gaussian curvature and its gradients across a surface. Our results imply that curvature and topology can be utilized to pattern defects in elastic materials, thus promising improved control over hierarchical bending, buckling, or folding processes. Generally, this study suggests that bilayer systems provide an inexpensive yet valuable experimental test bed for exploring the effects of geometrically induced forces on assemblies of topological charges.

DOI: 10.1103/PhysRevLett.116.104301

Topological defects and geometric frustration are intrinsic to two-dimensional (2D) curved crystals [1]. The minimal number of defects in a periodic polygonal tiling is dictated by Euler's theorem [2], which relates the surface geometry to the total topological defect charge. The hexagonal soccerball tiling is a canonical example, requiring 12 pentagonal defects that are also realized in C_{60} fullerenes [3]. However, large 2D crystals often exhibit defect numbers that go substantially beyond the minimal topological requirement [4]. These excess defects aggregate in moleculelike chains [5–7] that relieve elastic energy costs arising from a mismatch between the crystal symmetry and the curvature of the underlying manifold [8,9]. The aggregation of curvature-induced defects plays an essential role in various physical processes, from the classic Thomson problem of distributing discrete electric charges onto a sphere [10] to the assembly of virus capsules [11] and the fabrication of colloidosomes [12], toroidal carbon nanotubes [13], and spherical fullerenes from graphene [14]. Over the past decade, considerable progress has been made in understanding crystal formation in spherical [6,7,15] and more complex geometries [12,16–19]. Yet, empirical tests of theoretical concepts have remained restricted [5,20,21] to paraboloids or mean-curvature surfaces, owing to the lack of tractable experimental model systems.

Here, we show through theory and simulations that curved elastic bilayers offer a promising test bed to study defect crystallography in arbitrary 2D geometries. Building on a recently derived and experimentally validated scalar field theory [22], we first confirm that the pattern formation process induced by buckling of curved elastic films adhered to a softer substrate reproduces previously established

results for spherical crystals [6,23]. Subsequently, we demonstrate how curvature and topology determine defect localization on surfaces with nonconstant curvature. For typical experimental parameters [23], our analysis reveals the emergence of previously unrecognized robust superstructures, suggesting the usage of topology and geometry to control defect aggregation.

Our elastic bilayer system consists of a thin stiff film adhered to a soft curved substrate. Recent experiments [23–25] with spherical substrates showed that, under weak compression, such films can develop a buckled surface topography comprising a crystalline quilted pattern (Fig. 1). The experimental patterns are described quantitatively by a generalized Swift-Hohenberg theory [22], which is

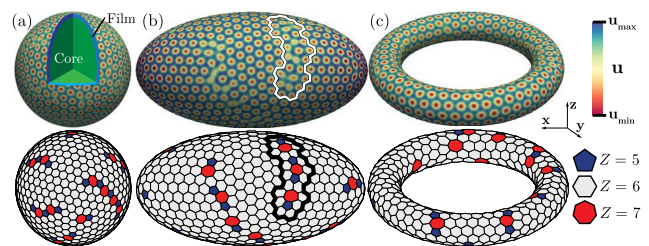


FIG. 1. Buckling-induced crystalline surface patterns on a thin film of thickness h adhered to a soft core (top), obtained by minimization of Eq. (1), and their dual hexagonal Voronoi tessellations (bottom) for different surface geometries: (a) sphere ($R/h = 70$), (b) ellipsoid ($R_x = 2R_y = 2R_z = 110h$), and (c) torus ($r/h = 16$, $R/h = 80$). The color bar represents the surface elevation. The outlined surface domain in (b) highlights a representative chain of defects. Voronoi cells are color coded by their coordination number Z .

employed here to obtain predictions for more general geometries. Measuring lengths in units of film thickness h and focusing on leading-order effects, the theory relates the normal displacement field u of the deformed film to the minimum of the energy functional [22]

$$\mathcal{E} = \frac{k}{2} \int_{\omega} d\omega \left[\gamma_0 (\nabla u)^2 + \frac{1}{12} (\Delta u)^2 + au^2 + \frac{c}{2} u^4 - \Gamma(u) \right], \quad (1)$$

where $k = E_f / (1 - \nu^2)$, and E_f is the Young's modulus of the film with undeformed surface element $d\omega$. The Poisson's ratio ν is assumed to be equal for the film and substrate. The nonlinear term $\Gamma(u) = 1/2[(1 - \nu)b^{\alpha\beta}\nabla_{\alpha}u\nabla_{\beta}u + 2\nu\mathcal{H}(\nabla u)^2]u + \mathcal{H}[4\mathcal{H}^2 - (3 - \nu)\mathcal{K}]u^3$ represents stretching forces, with surface gradient ∇ and Laplace-Beltrami operator Δ . The trace \mathcal{H} of the curvature tensor $b^{\alpha\beta}$ defines the mean curvature and \mathcal{K} denotes the Gaussian curvature. Periodic undulating patterns form on the surface when the film stress exceeds the critical buckling stress, corresponding to $a < a_c = 3\gamma_0^2$ where γ_0 defines the pattern wavelength $\lambda = 2\pi/\sqrt{6|\gamma_0|}$, while the amplitude is controlled by c [22]. The curvature-dependent $\Gamma(u)$ term determines the symmetry of the patterns. In the planar case with $\Gamma(u) = 0$, Eq. (1) reduces to the Swift-Hohenberg model [26] and minimization of Eq. (1) produces stripe patterns. For $|\Gamma(u)| > 0$, the symmetry $u \rightarrow -u$ is broken, causing a transition to hexagonal dimple patterns [22]. A systematic derivation [22] specified all parameters in Eq. (1) in terms of known material and geometric quantities, so that our predictions can be directly compared to future experiments. Our simulations use the material parameters of Ref. [22] for the hexagonal phase with $\lambda \sim 9.1$ throughout.

We analyze Eq. (1) for spheres of radius R , prolate ellipsoids of principal axis $R_x = 2R_y = 2R_z$, and tori with aspect ratio r/R between major axis R and minor axis r (Fig. 1). For each geometry, we choose $a/a_c \approx 0.98$ and

add small random perturbations to the originally undeformed film ($u_0 \equiv 0$). We then minimize Eq. (1) numerically using a custom-made finite element method [27]. From the stationary displacement field, the dimple centroids are identified as lattice points and the corresponding Voronoi tessellations are constructed (Fig. 1). We define the topological charge $s = 6 - Z$ for each lattice point, where Z is the coordination number. Probability density functions (PDFs) and statistical averages are obtained from simulations with different random initial conditions but otherwise identical parameters.

Since the total number of lattice units N is proportional to the surface area, \sqrt{N} is a geometry-independent measure of the system size. We now characterize the total number of defects N_d and find that it grows linearly with \sqrt{N} for all geometries [Fig. 2(a)], while generally exceeding the Euler bound for the minimal number of defects. For example, the case with the 12 topologically required defects of charge $s = +1$ (*positive disclinations*) can only be observed for small spheres, whereas N_d increases linearly with slope $m = 4.5 \pm 0.6$ above the critical size $\sqrt{N_c} = 14.2 \pm 3.6$ [Fig. 2(a)]. In terms of the reduced radius $\rho = R/\lambda$, N_c corresponds to a critical value $\rho_* \sim 4.3$, in good agreement with experiments [23].

The increase of N_d with system size can be explained as follows. Each disclination imposes a set change of Gaussian curvature, independently of \sqrt{N} . If the mismatch with the substrate's target curvature becomes too large, additional defects are introduced to screen curvature, thereby lowering the total elastic energy [9,28]. To preserve the total charge, excess defects appear as neutral pairs of opposite charge called *dislocations*. For large systems, defects typically form longer chains classified as either neutral *pleats* or charged *scars* [5]. For spheres, the number of excess dislocations per scar is predicted to grow linearly above ρ_c with slope $\approx 0.41\rho$ [9,28]. This scaling has been experimentally verified in colloidal crystals [6], and agrees with our simulations [solid line in the inset of Fig. 2(a)],

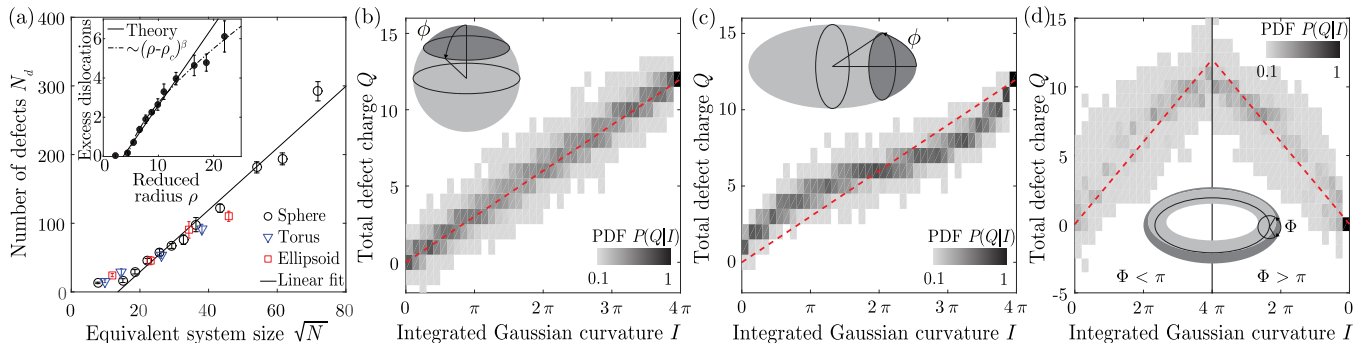


FIG. 2. (a) The total number of defects grows linearly with \sqrt{N} , where N is total number of lattice units, exhibiting similar slopes for all geometries (solid line: linear fit for spheres). Inset: Excess dislocations on spheres were predicted [6] to increase linearly with reduced radius $\rho = R/\lambda$ for colloidal crystals (solid line). For comparison, the best-fit power law $(\rho - \rho_c)^\beta$ with $\rho_c = 4.5 \pm 0.4$ and $\beta = 0.67 \pm 0.08$ is also shown (dashed line). (b)–(d) The total defect charge grows differently with integrated Gaussian curvature I for different geometries. The gray shading represents the conditional PDFs of the total charge Q for a given value of I . The red dashed line corresponds to linear growth $I = (\pi/3)Q$. Dark regions in the surface sketches illustrate integration domains.

although a power law $\sim(\rho - \rho_c)^\beta$ with $\rho_c = 4.5 \pm 0.4$ and $\beta = 0.67 \pm 0.08$ also fits our data well [Fig. 2(a), inset] [29]. These findings illustrate that geometry-induced defect formation is insensitive to the details of the lattice interactions [30], corroborating that elastic buckling patterns can provide a viable model to study generic aspects of curved crystals.

The screening effect of dislocations and its dependence on geometry become manifest in the relationship between Gaussian curvature and topological charge [5,23]. The Euler and Gauss-Bonnet theorems connect the sum of topological charges s_i for all elements, $Q = \sum_i s_i$, with the surface integral of the Gaussian curvature, $I = \int_A \mathcal{K} dA = \pi/3 \sum_i s_i = 2\pi\chi$, where χ is the Euler characteristic of the surface. How well this relationship is satisfied over a *subregion* of the surface provides insight into the geometry dependence of defect localization. For spheres, our results are consistent with the Gauss-Bonnet theorem; Q increases linearly with I [Fig. 2(b)]. By contrast, for ellipsoidal geometries, Q grows faster than I near the poles ($|\phi| = \pi/2$) and there is an accumulation of positive charges in high-curvature regions [Fig. 2(c)]. Although tori require no topological charge ($\chi = 0$), our simulations predict the creation of defects that help the dimpled crystal comply with the curved substrate geometry [16]. In the outer region of the torus, where Gaussian curvature is positive, we find that Q grows faster than linearly with I , which is qualitatively similar to the ellipsoidal case but with larger spread.

Another striking phenomenon is the curvature-induced localization and segregation of oppositely charged defects. For ellipsoids, we find that the PDF for angular position of positively charged disclinations increases strongly towards the poles, where for the chosen aspect ratio the local Gaussian curvature is equivalent to that of a smaller sphere with 2.6 times lower equivalent size. This explains why isolated defects can be found at the poles of even relatively large ellipsoids [Fig. 3(a)]. With increasing size, additional scars and pleats appear. Their centroid positions cluster in the equator region around $\phi = 0$ [Fig. 3(b)], where the curvature is low and thus cannot support isolated disclinations. To study the orientations of these extended defect “molecules,” we measure the orientation angle α enclosed by the end-to-end vector \mathbf{v} and the tangent \mathbf{t} along lines with $\theta = \text{const}$. We find no significant orientational order for positive or neutral chains [Figs. 3(b)–3(d)], consistent with earlier simulations based on an inflation packing algorithm [31].

Tori, in contrast to ellipsoids, contain regions of positive and negative curvature and are more prone to striped patterns. To identify the conditions for the pure crystal phase, we recall that hexagonal patterns require $|\Gamma(u)| > 0$ in Eq. (1), whereas local stripe solutions emerge otherwise [22]. The phase boundary at the onset of instability, $a = a_c$, can be estimated by parametrizing the torus using the standard coordinates (ϕ, θ) , then assuming a striped pattern symmetric along θ , and finally inserting $u(\theta, \phi) \equiv u(\phi)$

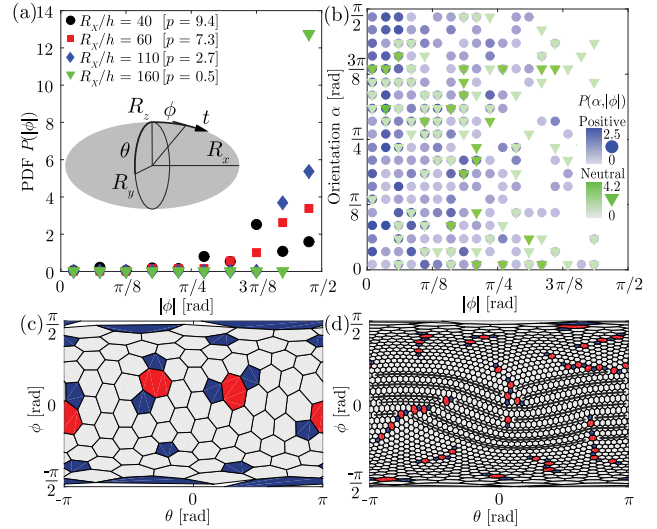


FIG. 3. Curvature-induced defect localization on ellipsoids. (a) Isolated pentagonal +1 defects accumulate in high curvature regions; p is the average number of single defects per ellipsoid. (b) Although defect chains form preferentially near the equator ($|\phi| = 0$) their orientation angles α , measured relative to the tangent vectors \mathbf{t} , show no significant ordering. (c),(d) Voronoi tessellations for $R_x/h = 40$ and $R_x/h = 160$. Ellipsoids with $R_x/h \geq 110$ show a weak alignment of the lattices along lines $\phi = 0$ (elements with the same lattice orientation are connected by solid black lines).

into the condition $\Gamma(u) = 0$. Solving for ϕ , we find (see Ref. [32] for the derivation details)

$$\phi_c \approx \pm \cos^{-1} \left[-\frac{R}{r(1+\nu)} \right], \quad (2)$$

which is independent of the system size and holds as long as $R, r \gg \lambda$. For rubberlike materials ($\nu \approx 0.5$) solutions $\pm\phi_c \in [(\pi/2), \pi]$ exist only for aspect ratios $r/R > 2/3$. We thus expect striped patterns to dominate near the inner rim of thick tori. Estimates of ϕ_c for $a < a_c$ can be obtained similarly from isolines of the normalized symmetry-breaking contribution to the energy density $\gamma(r/R, \phi) = (1 + r/R \cos \phi)(1 + \nu) - \nu$ [32]. To verify our predictions, we measured ϕ_c in simulations for tori with $0.2 \leq r/R \leq 0.8$ and $a/a_c = 0.98$ (see Ref. [32]), and find good agreement with the isoline $\gamma = 0.42$ [Fig. 4(a) and additional data in Ref. [32]]. The existence of a pure hexagonal phase for $r/R < 2/3$ provides a design guideline to study toroidal crystals in future experiments.

Focusing on crystalline patterns on slender tori with $r/R = 0.2$, our simulations show that defect localization is strongly controlled by the interplay of Gaussian curvature and topology. The requirement of a vanishing net charge implies that positive and negative disclinations appear in pairs. Their spatial arrangement can be rationalized with an electrostatic analogy [17], in which defects are interpreted as charged particles and curvature acts as an electric field. In this picture, positive disclinations are attracted to regions

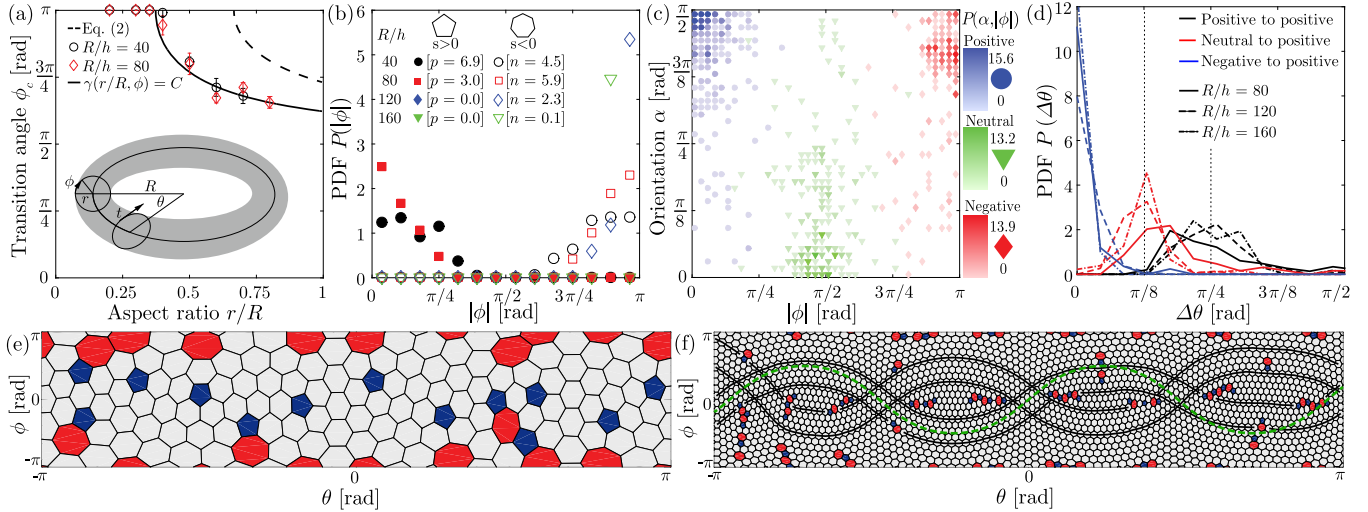


FIG. 4. Defect localization and superstructures on tori. (a) At the onset of instability, $a = a_c$, pure hexagonal phases are stable only for tori with $r/R < 2/3$ (dashed line, Eq. 2), while striped patterns occur at angles $\phi > \phi_c$ for larger aspect ratios. Simulations for $a/a_c = 0.98$ agree well with the isoline estimates of the symmetry-breaking terms in the energy density, $\gamma(r/R, \phi) = C$, with $C = 0.42$ (solid line). (b) Isolated penta- and heptagonal defects segregate; p and n are the average numbers of positive and negative disclinations per torus. (c) Orientations of charged scars and neutral pleats correlate strongly with their transversal centroid position $|\phi|$. (d) Defect positions are also strongly correlated along θ . (e),(f) While this positional ordering is less prominent in small systems [(e), $R/h = 40$], it becomes apparent for larger systems [(f) $R/h = 160$]. The toroidal superstructure (elements with the same lattice orientation are connected by solid black lines) follows geodesics of minimal integrated absolute Gaussian curvature (dashed green line).

of positive Gaussian curvature at the outer rim of the torus ($\phi = 0$), whereas negative disclinations migrate to the inner region ($|\phi| = \pi$). This geometry-induced separation of charges is directly reflected in the PDF of the individual disclinations [Fig. 4(b)]. Analogously to the ellipsoidal case, the total number of isolated disclinations [see the average numbers p and n for positive and negative charges in Fig. 4(b)] decreases with system size, as defects tend to aggregate in chains [Figs. 4(e) and 4(f)]. Interestingly, we find that the electrostatic analogy extends to defect chains: positive scars screen Gaussian curvature on the outer rim; negative scars appear in the inner region; and neutral pleats concentrate in the regions of vanishing Gaussian curvature, $|\phi| = \pi/2$ [Fig. 4(c)]. Defect chains also become oriented by geometric forces. Measuring the orientation angle α of a chain relative to the tangent vector \mathbf{t} along the ϕ direction [Fig. 4(a)], we find that charged scars preferentially align parallel to the equatorial lines such that $\alpha \sim \pi/2$, whereas neutral pleats tend to orient vertically with $\alpha \sim 0$ [Fig. 4(c)]. This ordering can be understood qualitatively by considering the end points of a defect chain. For scars, both end points have the same charge and therefore migrate to regions of same Gaussian curvature ($\phi \sim 0$ for positively charged end points, $\phi \sim \pi$ for negatively charged ones), effectively orienting the scar perpendicular ($\alpha = \pi/2$) to lines $\phi = \text{const}$. By contrast, pleats have oppositely charged ends and hence mimic electric dipoles that become oriented by curvature to achieve $\alpha = 0$.

Remarkably, our simulations reveal that defects not only orient and segregate in the torus curvature field—they also break the rotational symmetry of the toroidal crystal in favor of an emergent discrete symmetry. More precisely, by

analyzing the lattice structure on large tori, we find that the hexagonal elements arrange along an undulating periodic deformation pattern [highlighted in Fig. 4(f) by the black lines connecting the centroids of elements with the same lattice orientation]. This superstructure still carries a fingerprint of the underlying toroidal geometry: geodesics $\mathbf{g}(\phi) = (\phi, \theta(\phi))$ on a torus are solutions of [35]

$$\frac{d\theta}{d\phi} = \frac{cr}{(R + r \cos \phi) \sqrt{(R + r \cos \phi)^2 - c^2}}. \quad (3)$$

where c is a constant obeying Clairaut's geodesic relation $c = (R + r \cos \phi) \sin \psi$, with ψ denoting the angle between the tangent \mathbf{g}' and \mathbf{t} [35]. Integrating Eq. (3) numerically, we find that the lattice deformation follows a geodesic passing through $\phi = 1.68$ at its highest point with $\psi = \pi/2$ [dashed green line in Fig. 4(f)]. The phase θ_0 , found by matching the phase of the geodesic with that of the lattice, varies between samples. The integrated absolute Gaussian curvature along this curve is minimal among all geodesics that do not wind around the ϕ coordinate. We therefore hypothesize that alignment along a geodesic of minimal absolute Gaussian curvature yields an energetically favorable crystal structure, for *at least* those lattice parts close to where the geodesic remain nearly straight—much like wrapping a torus with an inextensible ribbon. If this geometric argument is correct, the superstructure should become independent of the lattice size, as R/h increases. To test this hypothesis, we simulated system sizes $R/h \in \{80, 120, 160\}$, and measured the angular distance $\Delta\theta$ between positive scars near the outer rim. These simulations indeed reveal a peak in the PDF $P(\Delta\theta)$ near $\pi/4$, which corresponds to one-quarter of the geodesic wavelength,

independently of system size [Fig. 4(d), black curves]. Moreover, negative scars on the inside of the torus appear in phase with positive scars ($\Delta\theta = 0$), while neutral pleats arrange between scars ($\Delta\theta \sim \pi/8$). Thus, the geometric lattice superstructure also controls defect-chain localization.

A significant advantage of elastic surface crystals over fluid-based systems is their fabrication versatility, which enables the exploration of arbitrary geometries and topologies. Of particular biomedical and nanotechnological relevance are toroidal geometries that are difficult to achieve in a colloidal suspension. Important realizations include toroviruses [12] and carbon nanotori [13], whose electromagnetic properties are affected by defects [36,37]. Our results show that spatially varying curvature can lead to emergent superstructures that determine defect localization. Since defects trigger secondary instabilities [38], this previously unrecognized phenomenon may be also exploited to control hierarchical buckling and folding. More generally, our analysis implies that elastic surface crystals provide a rich model system for studying the profound interplay between geometric forces and topological charges.

We thank Mark Bathe for sharing computational facilities. This work was supported by the MIT and Masdar Institute Cooperative Program (F. L. J.), the Swiss National Science Foundation, 148743 (N. S.), an MIT Solomon Buchsbaum Fund Award (J. D.), an Alfred P. Sloan Research Fellowship (J. D.), and by the National Science Foundation, CAREER CMMI-1351449 (P. M. R.).

F. L. J., N. S., and R. L. contributed equally to this work.

*Corresponding author.
dunkel@mit.edu

†Corresponding author.
preis@mit.edu

- [1] J.-F. Sadoc and R. Mosseri, *Geometrical Frustration* (Cambridge University Press, Cambridge, England, 2006).
- [2] L. Euler, *Novi Comment. Acad. Sci. Imp. Petropol.* **4**, 109 (1758).
- [3] H. W. Kroto, J. R. Heath, S. C. O'Brien, R. F. Curl, and R. E. Smalley, *Nature (London)* **318**, 162 (1985).
- [4] M. J. W. Dodgson and M. A. Moore, *Phys. Rev. B* **55**, 3816 (1997).
- [5] W. Irvine, V. Vitelli, and P. Chaikin, *Nature (London)* **468**, 947 (2010).
- [6] A. Bausch, M. Bowick, A. Cacciuto, A. Dinsmore, M. Hsu, D. Nelson, M. Nikolaides, A. Travesset, and D. Weitz, *Science* **299**, 1716 (2003).
- [7] T. Einert, P. Lipowsky, J. Schilling, M. Bowick, and A. Bausch, *Langmuir* **21**, 12076 (2005).
- [8] A. Pérez-Garrido, M. J. W. Dodgson, and M. A. Moore, *Phys. Rev. B* **56**, 3640 (1997).
- [9] M. J. Bowick, D. R. Nelson, and A. Travesset, *Phys. Rev. B* **62**, 8738 (2000).
- [10] J. Thomson, *Philos. Mag.* **7**, 237 (1904).
- [11] D. Caspar and A. Klug, *Quant. Biol.* (Cold Spring Harbor Laboratory Press, Cold Spring Harbor, NY, 1962), Vol. 27, p. 1; E. Snijder and M. Horzinek, *J. Gen. Virol.* **74**, 2305 (1993).
- [12] A. Dinsmore, M. Hsu, M. Nikolaides, M. Marquez, A. Bausch, and D. Weitz, *Science* **298**, 1006 (2002); V. Manoharan, *Science* **349**, 1253751 (2015).
- [13] J. Liu, H. Dai, J. H. Hafner, D. T. Colbert, and R. E. Smalley, *Nature (London)* **385**, 780 (1997).
- [14] A. Chuvilin, U. Kaiser, E. Bichoutskaia, N. Besley, and A. Khlobystov, *Nat. Chem.* **2**, 450 (2010).
- [15] D. J. Wales and S. Ulker, *Phys. Rev. B* **74**, 212101 (2006).
- [16] L. Giomi and M. J. Bowick, *Eur. Phys. J. E* **27**, 275 (2008).
- [17] M. Bowick, D. R. Nelson, and A. Travesset, *Phys. Rev. E* **69**, 041102 (2004).
- [18] E. Bendito, M. J. Bowick, A. Medina, and Z. Yao, *Phys. Rev. E* **88**, 012405 (2013). V. Vitelli, J. B. Lucks, and D. R. Nelson, *Proc. Natl. Acad. Sci. U.S.A.* **103**, 12323 (2006).
- [19] C. Negri, A. Sella, S. Zapperi, and M. Miguel, *Proc. Natl. Acad. Sci. U.S.A.* **112**, 14545 (2015).
- [20] M. J. Bowick, L. Giomi, H. Shin, and C. K. Thomas, *Phys. Rev. E* **77**, 021602 (2008).
- [21] W. Irvine, M. Bowick, and P. Chaikin, *Nat. Mater.* **11**, 948 (2012).
- [22] N. Stoop, R. Lagrange, D. Terwagne, P. Reis, and J. Dunkel, *Nat. Mater.* **14**, 337 (2015).
- [23] M. Brojan, D. Terwagne, R. Lagrange, and P. Reis, *Proc. Natl. Acad. Sci. U.S.A.* **112**, 14 (2015).
- [24] D. Terwagne, M. Brojan, and P. M. Reis, *Adv. Mater.* **26**, 6608 (2014).
- [25] D. Breid and A. J. Crosby, *Soft Matter* **9**, 3624 (2013).
- [26] M. C. Cross and P. C. Hohenberg, *Rev. Mod. Phys.* **65**, 851 (1993).
- [27] N. Stoop, F. K. Wittel, M. B. Amar, M. M. Müller, and H. J. Herrmann, *Phys. Rev. Lett.* **105**, 068101 (2010); R. Vetter, N. Stoop, T. Jenni, F. K. Wittel, and H. J. Herrmann, *Int. J. Numer. Methods Eng.* **95**, 791 (2013).
- [28] A. Travesset, *Phys. Rev. B* **68**, 115421 (2003).
- [29] We consider a dislocation to be part of a scar when the distance is smaller than or equal to two lattice spacings.
- [30] M. Bowick, A. Cacciuto, D. R. Nelson, and A. Travesset, *Phys. Rev. Lett.* **89**, 185502 (2002).
- [31] C. J. Burke, B. L. Mbanga, Z. Wei, P. T. Spicer, and T. J. Atherton, *Soft Matter* **11**, 5872 (2015).
- [32] See Supplemental Material at <http://link.aps.org/supplemental/10.1103/PhysRevLett.116.104301>, which includes Refs. [33,34], for the derivation of the equations in the main text and further details on the alignment of the toroidal crystal.
- [33] E. Abbena, S. Salamon, and A. Gray, *Modern Differential Geometry of Curves and Surfaces with Mathematica* (CRC Press, Boca Raton, 2006).
- [34] A. A. Golovin and A. A. Nepomnyashchy, *Self-Assembly, Pattern Formation and Growth Phenomena in Nano-Systems* (Springer, Dordrecht, 2006).
- [35] J. Oprea, *Differential Geometry and Its Applications* (Mathematical Association of America, Oberlin, OH, 2007).
- [36] Z. Zhang, Z. Yang, X. Wang, J. Yuan, H. Zhang, M. Qiu, and J. Peng, *J. Phys. Condens. Matter* **17**, 4111 (2005).
- [37] J. A. Rodríguez-Manzo, F. López-Urías, M. Terrones, and H. Terrones, *Small* **3**, 120 (2007).
- [38] E. H. Yong, D. R. Nelson, and L. Mahadevan, *Phys. Rev. Lett.* **111**, 177801 (2013).

Supplemental Material:

Curvature-controlled defect localization in elastic surface crystals

Francisco López Jiménez,^{1,*} Norbert Stoop,^{2,*} Romain Lagrange,^{2,*} Jörn Dunkel,² and Pedro M. Reis^{1,3}

¹*Department of Civil & Environmental Engineering, Massachusetts Institute of Technology,
77 Massachusetts Avenue, Cambridge, MA 02139-4307, USA*

²*Department of Mathematics, Massachusetts Institute of Technology,
77 Massachusetts Avenue, Cambridge, MA 02139-4307, USA*

³*Department of Mechanical Engineering, Massachusetts Institute of Technology,
77 Massachusetts Avenue, Cambridge, MA 02139-1713, USA*

(Dated: February 10, 2016)

SI. WRINKLING ON CURVED GEOMETRIES

The wrinkling of a thin, compressed film adhering to a curved substrate can effectively be described by a Swift-Hohenberg-like scalar field equation. Measuring all lengths in terms of the film thickness h , the associated elastic energy is given by (Eq. 33b in the Supplementary Information, SI, of Ref. [1]):

$$\begin{aligned} \mathcal{E} = \frac{k}{2} \int_{\omega} d\omega & \left[\frac{\gamma_0}{2} (\nabla u)^2 + \frac{\gamma_2}{2} (\Delta u)^2 + \frac{a}{2} u^2 + \frac{b}{3} u^3 + \frac{c}{4} u^4 - \right. \\ & \frac{1}{2} [(1-\nu)b^{\alpha\beta} \nabla_{\alpha} u \nabla_{\beta} u + 2\nu \mathcal{H}(\nabla u)^2] u + \\ & \left. \frac{1}{4} [(1-\nu)c^{\alpha\beta} \nabla_{\alpha} u \nabla_{\beta} u + \nu \mathcal{K}(\nabla u)^2] u^2 \right]. \quad (\text{S1}) \end{aligned}$$

Here, the parameter a is linked to the film stress and plays the role of a bifurcation parameter: increasing the film stress reduces a and bifurcation from an unwrinkled to a wrinkled film eventually occurs for $a/a_c < 1$ with a_c as defined in the Main Text. $b^{\alpha\beta}$ is the curvature tensor, and \mathcal{H} and \mathcal{K} are the mean and Gaussian curvature, respectively. Eq. (1) of the Main Text is obtained from Eq. (S1) above by identifying $b = -3\mathcal{H}(\mathcal{H}^2 - (3-\nu)\mathcal{K})$ [1], $\Gamma(u) = \frac{1}{2} [(1-\nu)b^{\alpha\beta} \nabla_{\alpha} u \nabla_{\beta} u + 2\nu \mathcal{H}(\nabla u)^2] u - \frac{b}{3} u^3$ and by neglecting the term on the third line involving the third fundamental form $c^{\alpha\beta}$, which we numerically found to be irrelevant for the pattern formation for the pattern formation process.

In the following, we consider toroidal geometries, noting that the procedure is analogous for other surfaces. Parametrizing a torus of major radius R and minor radius r by $\mathbf{X} = [(R+r \cos \phi) \cos \theta, (R+r \cos \phi) \sin \theta, r \sin \phi]$ with coordinates $(\theta, \phi) \in [0, 2\pi) \times [0, 2\pi)$ yields [1, 2]

$$(a_{\alpha\beta}) = \begin{pmatrix} (R+r \cos \phi)^2 & 0 \\ 0 & r^2 \end{pmatrix} \quad (\text{S2a})$$

$$(b^{\alpha\beta}) = - \begin{pmatrix} \cos \phi (R+r \cos \phi)^{-3} & 0 \\ 0 & r^{-3} \end{pmatrix} \quad (\text{S2b})$$

$$d\omega = \sqrt{J} d\theta d\phi \quad (\text{S3a})$$

$$\sqrt{J} = \sqrt{|\det\{a_{\alpha\beta}\}|} = R^2 \tau (1 + \tau \cos \phi) \quad (\text{S3b})$$

$$\mathcal{H} = -\frac{1 + 2\tau \cos \phi}{2r(1 + \tau \cos \phi)}, \quad \mathcal{K} = \frac{\cos \phi}{rR(1 + \tau \cos \phi)} \quad (\text{S3c})$$

where we used $\tau = r/R$. Subscripts denote covariant components, while superscripts denote contravariant components. Indices are raised using the inverse metric with components $a^{\alpha\beta}$.

The interplay between the symmetry-breaking term $\Gamma(u)$ and the bifurcation parameter a determines the wrinkling morphology [1]. Classical nonlinear analysis of the planar Swift-Hohenberg equation predicts a global hexagonal phase in presence of a symmetry-breaking cubic energy term γu^3 , with γ constant. It is known that the hexagonal phase remains stable in a regime $1-\epsilon < a/a_c < 1$ of the bifurcation parameter a ; the width of this regime is $\epsilon \sim \gamma^2$ [3]. In our wrinkling model, a relates to the film stress, and Γ scales with the curvature tensor: qualitatively, hexagons are stable if the film stress is sufficiently small and curvature is sufficiently high [1].

For toroidal geometries, the symmetry-breaking term depends on the position coordinate ϕ . We therefore consider the local energy contribution $\Gamma(u)\sqrt{J}$, which takes into account the ϕ -dependence of the area element via the surface Jacobian \sqrt{J} . We assume that the wrinkling pattern u consists of an axisymmetric, stripe-like solution with fixed wavelength $\lambda = 2\pi/k_c$, i.e. $u \equiv u(\phi) = A \exp(ik_c r \phi)$. Inserting this ansatz into $\Gamma(u)\sqrt{J}$ and noting that $\nabla_1 u = 0$ and $\nabla_2 u = ik_r u$, and together with Eqs. (S3), we obtain after some algebraic simplifications,

$$\Gamma(u)\sqrt{J} = \left[\frac{2(\pi R)^2}{\lambda^2} [(1 + \tau \cos \phi)(1 + \nu) - \nu] - A \right] \frac{u^3}{R}, \quad (\text{S4})$$

$$A = \frac{(1 + 2\tau \cos \phi) [1 + \tau \cos \phi (1 + \nu) (1 + \tau \cos \phi)]}{2\tau^2 (1 + \tau \cos \phi)^2}. \quad (\text{S5})$$

Noting that $(\lambda/R)^2 \ll 1$ for all the systems we consider, the first term in Eq. (S4) dominates. Neglecting

* These authors contributed equally to this work.

the second term A , we obtain

$$\Gamma(u)\sqrt{J} \approx \frac{2\pi^2 R}{\lambda^2} \gamma(\tau, \phi) u^3 \quad (\text{S6})$$

$$\gamma(\tau, \phi) = (1 + \tau \cos \phi)(1 + \nu) - \nu \quad (\text{S7})$$

As in the classical planar Swift-Hohenberg analysis, we expect stable hexagons at the onset of the bifurcation if $\gamma(\tau, \phi) \neq 0$, and labyrinths where $\gamma(\tau, \phi) = 0$. Solving the latter condition (or equivalently $\Gamma(u) = 0$) for ϕ immediately leads to Eq. (2) of the Main Text.

Beyond bifurcation, hexagons are expected to be stable wherever $|\Gamma(u)|\sqrt{J}$ is large enough to support them, i.e. $\gamma(\tau, \phi) > C$ for some C that depends on the bifurcation parameter a . Although the precise relationship between a and C is unknown, the isolines of $\gamma(\tau, \phi)$ provide a qualitative picture of the phase transition lines for different choices of a (Fig. S1). To confirm these predictions, we simulated tori of varying aspect ratios τ and different film stresses. Defining the critical transition angle ϕ_c in the simulations as the angle beyond which less than half of the wrinkled surface takes the form of hexagonal dimples, we find good agreement with the isoline predictions for small film stresses (black, blue and green symbols in Fig. S1). It should be noted that it is numerically challenging to prepare a system precisely at the onset $a = a_c$, so that we cannot reproduce the 0-isoline of Eq. (2) of the Main Text (dashed line in Fig. S1). As the film stress is increased, our simulations reveal a distinct peak of ϕ_c around $r/R \approx 0.4$ (magenta symbols in Fig. S1). Qualita-

tively, this behavior is predicted by the isoline approach, although the peak is located at considerably smaller r/R . A potential explanation for this deviation comes from the fact that in our systems, $\lambda \sim 9.1$ and $R/h = 40$. For small aspect ratios τ , only a few wrinkling patterns can fit on the torus along the minor circle, so that ϕ_c can only be measured approximately.

S2. CRYSTALLOGRAPHIC ALIGNMENT ALONG TOROIDAL SUPERSTRUCTURE

In Fig. S2, we provide additional evidence for the alignment of our toroidal crystals along a superstructure. To this end, we considered the time evolution of the crystal formation process, which we obtained by minimizing the energy on Eq. (1) of the Main Text using overdamped dynamics with fixed time step Δt , analogously to the method presented in Ref. [1]. Using local Voronoi cell reconstruction, Fig. S2 shows that the crystallization is initiated from different condensation sites. Despite being disconnected initially, individual crystallization sites already grow along the superstructure at early times (Fig. S2, \mathbf{t}_1), resembling the global crystal alignment found for growing colloidal crystals on spherical substrates [4]. When originally disconnected crystallization zones merge at later time steps, defects form along their common boundaries (Fig. S2, \mathbf{t}_2 and \mathbf{t}_3). Further minimization of the elastic energy leads to annihilation of defects (Fig. S2, \mathbf{t}_4), resulting in the final equilibrated crystal (Fig. S2, \mathbf{t}_4).

-
- [1] N. Stoop, R. Lagrange, D. Terwagne, P. Reis, and J. Dunkel, *Nat. Mat.* **14**, 337 (2015).
 [2] E. Abbena, S. Salamon, and A. Gray, *Modern differential geometry of curves and surfaces with Mathematica* (CRC press, 2006).

- [3] A. A. Golovin and A. A. Nepomnyashchy, *Self-assembly, pattern formation and growth phenomena in nano-systems* (Springer, Dordrecht, 2006).
 [4] C. Negri, A. Sellaio, S. Zapperi, and M. Miguel, *Proc. Natl. Acad. Sci. U.S.A.* **112**, 14545 (2015).

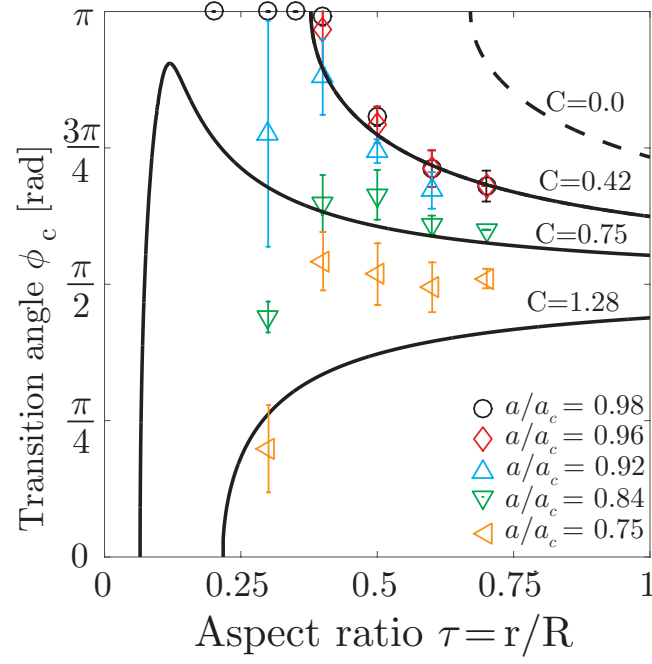


FIG. S1. (color online) Isolines of the symmetry-breaking term, $\gamma(\tau, \phi) = C$, approximate local wrinkling pattern transitions on toroidal geometries. At the wrinkling onset $a = a_c$, pure hexagonal wrinkling phases are stable only for tori with $r/R < 2/3$ (dashed line, Eq. 2 Main Text), while stripe-like patterns occur at angles $\phi > \phi_c$ for larger aspect ratios. Simulations for $a/a_c = 0.98$ (black symbols) agree well with the isoline estimates of the symmetry-breaking energy density, $\gamma(r/R, \phi) = C$, with $C = 0.42$ (solid line). Additional simulations are included for higher film stresses with $a/a_c = 0.96$ (red), $a/a_c = 0.92$ (blue), $a/a_c = 0.84$ (green), and $a/a_c = 0.75$ (orange).

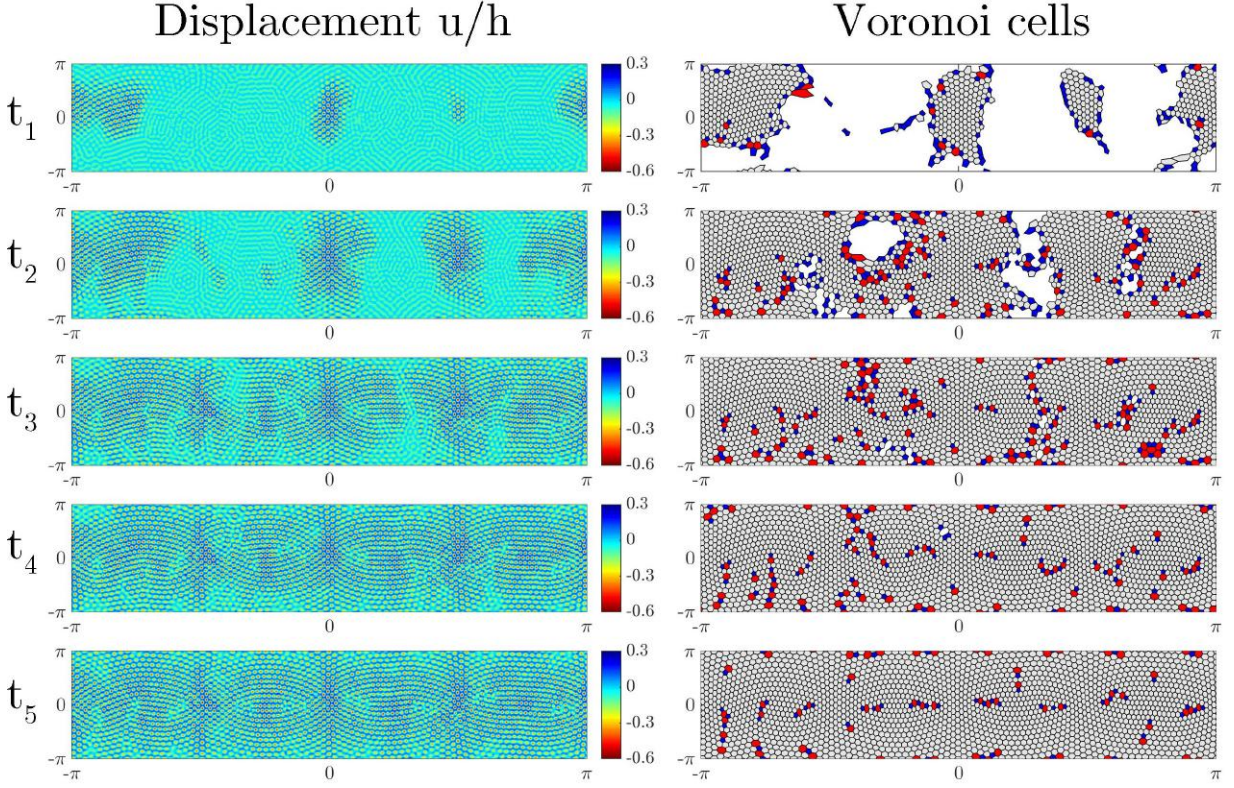


FIG. S2. Time evolution of the displacement field u/h (left) and the corresponding Voronoi cells (right) at different succeeding snapshots in time ($t_1 = 22000$, $t_2 = 24000$, $t_3 = 26000$, $t_4 = 32000$, and $t_5 = 2800400$, time increment per iteration $\Delta t = 40$). Remarkably, the alignment of the crystal along an undulating structure is already apparent at early stages of crystal formation (t_1). Defects initially appearing at the boundaries between merging crystallization zones (t_2 and t_3), but later annihilate to result in the final, equilibrated defect pattern (t_4).